
SUPPLEMENTARY INFORMATION: RAPID FLIPPING BETWEEN ELECTROLYTE AND METALLIC STATES IN AMMONIA SOLUTIONS OF ALKALI METALS

Marco Vitek¹, Igor Rončević^{1, 2, 3}, Ondrej Marsalek^{*4}, H. Christian Schewe^{*1, 5}, and Pavel Jungwirth^{*1}

¹Institute of Organic Chemistry and Biochemistry of the Czech Academy of Sciences, Flemingovo nám. 2, 166 10
Prague 6, Czech Republic

²Department of Chemistry, University of Oxford, Chemistry Research Laboratory, Mansfield Road, Oxford OX1 3TA,
UK

³Department of Chemistry, University of Manchester, Oxford Road, Manchester M13 9PL, UK

⁴Charles University, Faculty of Mathematics and Physics, Ke Karlovu 3, 121 16 Prague 2, Czech Republic

⁵J. Heyrovský Institute of Physical Chemistry, Czech Academy of Sciences, Dolejškova 3, 18223 Prague, Czech
Republic

April 3, 2025

Contents

Suppl. Note 1. Computational setup and methodology	2
Suppl. Note 1.1 Initial force-field pre-equilibration	2
Suppl. Note 1.2 AIMD methodology	2
Suppl. Note 1.3 Electronic structure calculations	3
Suppl. Note 1.4 Transport properties	3
Suppl. Note 1.5 Excess electron density	3
Suppl. Note 1.6 Interpolation of band eigenvalues	3
Suppl. Note 1.7 Generation of the spherical band structures	3
Suppl. Note 2. Methodology validation	5
Suppl. Note 2.1 Choice of density functional	5
Suppl. Note 2.2 GW convergence	10
Suppl. Note 3. Extended data analysis	12
Suppl. Note 4. Experimental photoelectron spectra and fitting procedures	17
Suppl. Note 4.1 Comparison of calculated DoS versus measured PE spectra	17
Suppl. Note 5. Supplementary data and analysis — revPBE0-D3 trajectories	21
Suppl. Note 5.1 Spherical band structures	21

Suppl. Note 5.2 Fluctuations in DoS	22
Suppl. Note 5.3 Excess electron density	24
Suppl. Note 5.4 Experimental validation	26
Suppl. Note 5.5 Correlations	28

Suppl. Note 1. Computational setup and methodology

In our study, we investigated systems comprised of 64 ammonia molecules with varying concentrations of solvated dielectrons and Li^+ cations: a concentration of 3.0 MPM corresponding to 1 dielectron (2 Li^+) in a 14.241 Å box, 6.0 MPM for 2 dielectrons (4 Li^+) in a 14.486 Å box, 11.1 MPM for 4 dielectrons (8 Li^+) in a 14.975 Å box, and 13.5 MPM for 5 dielectrons (10 Li^+) in a 15.218 Å box. Our simulations utilize periodic boundary conditions, introducing periodicity to model the infinite nature of the system and ensure convergence in k -point sampling. This approach, while essential for computational simulations, differs from real experiments where systems are not inherently periodic. The target volumes of the simulation boxes were estimated from the experimental density of liquid lithium ammonia solutions [1].

Initially, the systems were pre-equilibrated using force-field molecular dynamics (FFMD), see section Suppl. Note 1.1, where bromine anions served as placeholders for dielectron cavities. We ran four trajectories per system, each lasting 5 nanoseconds.

Next, we proceeded with *ab initio* molecular dynamics (AIMD), as detailed in section Suppl. Note 1.2, excluding the bromine anions. During this phase, four trajectories were generated for each system, consisting of roughly 2 ps of equilibration followed by 3–5 ps of production run per trajectory. The total production run durations for the 3.0, 6.0, 11.1, and 13.5 MPM systems were 19.70, 12.57, 13.53, and 13.97 ps, respectively.

To investigate the density of states (DoS) fluctuations in the 3.0, 6.0, 11.1, and 13.5 MPM systems, we sampled 500 different configurations at 2-femtosecond intervals per concentration. These samples were analysed using the revPBE38-D3 functional (the same functional as used for the AIMD that generated the trajectories) on a $2 \times 2 \times 2$ k -point mesh. Each series of analyses covered 1000 fs of trajectory. For each snapshot, transport properties were also calculated — see section Suppl. Note 1.4.

To identify potential structural differences between metallic and electrolyte states in electron density distribution of individual dielectrons, we conducted 500 revPBE38-D3 Γ -point calculations (section Suppl. Note 1.5) for the 3.0 MPM trajectory, taken at 2-femtosecond intervals.

For the analysis of solvated electron density distributions across the entire EMT range (3.0–13.5 MPM), we conducted 3940, 2514, 2706 and 2794 revPBE38-D3 Γ point calculations sampled at 5-femtosecond intervals from the 3.0, 6.0, 11.1, and 13.5 MPM AIMD trajectories (propagated in NVE ensemble with revPBE38-D3 functional).

To analyse the electron energy dispersion in momentum space, we developed a specialised tool to generate the spherical band structure (SBS) from a given DoS calculation — details are given in section Suppl. Note 1.7.

Suppl. Note 1.1 Initial force-field pre-equilibration

To obtain structurally realistic ensemble samples to serve as initial structures for *ab initio* molecular dynamics (AIMD) equilibration, we first conducted empirical force field molecular dynamics (FFMD) simulations. Interaction parameters were defined using the liquid-adapted ammonia force field (FF) [2]. The Gromacs software [3] was employed for the following identical procedures in all investigated systems:

1. Assembling the respective systems.
2. Conducting a 5.0 ns canonical MD equilibration at 235 K for each concentration. From the equilibrated trajectories of each system, four snapshots were selected to initiate additional FFMD simulations.
3. Executing four additional FFMD simulations for each set of snapshots, with each running for 5 ns in the canonical (NVT) ensemble at the same temperature as in step (2).

Suppl. Note 1.2 AIMD methodology

Explicit electronic structure calculations are needed for further equilibration and production simulations using AIMD. This was realized using the VASP program package [4–7] (version 6.3.2). Here, we used the hybrid revPBE38 [8–11]

density functional with the D3 dispersion correction [11, 12] selectively turned off for Li^+ cations [13]. Projector augmented-wave (PAW) pseudopotentials [14, 15] with the kinetic energy cutoff of 400 eV were used. Additionally, we used the smallest possible FFT grid that just encloses the cutoff sphere used in the exact exchange routines and softened augmentation charges. The propagation of nuclei was realised with a 0.5 fs time step. We ran the initial equilibration in the canonical ensemble at a temperature of 235 K (ca. -38°C) using a Langevin thermostat [16] with a 50 fs time constant. For the subsequent production simulation, we switched to a micro-canonical ensemble (NVE).

Suppl. Note 1.3 Electronic structure calculations

An accurate description of the electronic structure in periodic calculations requires a rigorous account of Coulombic screening. To obtain accurate quasiparticle band gaps and the frequency-dependent dielectric function, including electron–electron and electron–hole interactions, we employed the *GW* method [17, 18]. In (range-separated) hybrid DFT, the screening is strongly affected by the amount (or the decay) of exact exchange admixed parametrically into the employed density functional, making their results potentially unreliable without validation [19]. In contrast, in the *GW* approximation, the screened Coulombic interaction W is constructed *ab initio*, from the independent-particle polarisability, resulting in a significant improvement in band energies. It is therefore not surprising that *GW* has become the method of choice for computational photoelectron spectroscopy in a wide variety of systems [20–24].

To prepare for *GW* calculations, we first performed DFT calculations using the revPBE functional to approximate the exchange–correlation energy. These calculations employed PAW potentials and a plane-wave basis set with a kinetic energy cutoff of 400 eV, sampled using a $2\times 2\times 2$ Monkhorst-Pack k -point mesh [25], with Gaussian-type Fermi level smearing applied at a width of 0.075 eV. To refine the electronic structure, a follow-up DFT calculation was performed using the hybrid functional revPBE38, which includes 37.5 % exact exchange. The resulting revPBE38 wave function served as the reference for the *GW* calculations. This step ensures more accurate quasiparticle corrections by providing a high-quality starting point.

We then applied the *GW* method perturbatively, using the G_0W_0 (“single shot”) method, to obtain first-order corrections to the Kohn–Sham eigenvalues. The reference wave functions used as a starting point for the *GW* were obtained from revPBE38-D3 DFT calculations as described in the preceding paragraph. For all G_0W_0 calculations, we used a k -point mesh of $2\times 2\times 2$ and a number of empty bands that were at least 4 times the number of electrons in the simulation cell (2240 bands). The quasiparticle energies were evaluated for the 320 lowest bands. The energy cutoff for the response function was set to 100 eV. The number of (imaginary) frequency and imaginary time grid points was set to 100. The Gaussian-type Fermi level smearing method was used with a smearing width of 0.075 eV.

Suppl. Note 1.4 Transport properties

We calculated the thermoelectric properties based on either DFT (revPBE38-D3) or G_0W_0 band eigenvalues and Boltzmann transport theory using the BoltzTraP2 code, which uses the rigid band approach to calculate the transport coefficients [26, 27].

Suppl. Note 1.5 Excess electron density

Unlike single solvated electrons, for which the spin density can be used to characterise their spatial distribution, the (spin-paired) dielectron does not permit such characterisation [28]. Given our focus on concentrations where only dielectrons are present [29], we, therefore, utilised squares of maximally localised Wannier orbitals obtained from revPBE38-D3 gamma-point calculations to represent the excess electron density. These were calculated using the WANNIER90 program package [30], interfaced to VASP.

Suppl. Note 1.6 Interpolation of band eigenvalues

We employed the smooth Fourier interpolation method, as implemented in Boltztrap2 [26, 27], to interpolate the band eigenvalues. This results in a more detailed and higher-resolution representation of the DoS than what is provided by the initial coarse $2\times 2\times 2$ k -point mesh.

Suppl. Note 1.7 Generation of the spherical band structures

The band structure of a material describes the relationship between the energy of electrons and their momentum. In crystalline solids, this relationship is usually represented by plotting energy bands $E(k)$ along high-symmetry lines in the first Brillouin zone, a unit cell in momentum space. However, in disordered or liquid metals, the first Brillouin zone cannot be rigorously defined [31–34], and radial (in 2D systems) or spherical (3D) band structures are used. In such

cases, the energy-momentum relationship is represented in a spherically symmetric space, i.e. the electron energy is plotted versus the magnitude of k . Such a representation provides information not only about the electron energy, but also the extent of their (de)localisation in real space (i.e. flat bands correspond to localised states).

We developed a specialised tool to analyse electronic energy dispersion of disordered or liquid systems. Central to its functionality is the generation of spherical band structure (SBS). First, we calculated the electron detachment and attachment energies as a function of the wave-vector magnitude using revPBE38-D3 or the G_0W_0 method [17, 18]. Our tool then employs a Fourier expansion of band energies, as implemented in Boltztrap2 [26], to accurately interpolate band structures across energy levels and k -points in reciprocal space in 3D. Specifically, we begin by generating band structures in spherical coordinates from Γ -point centred k -point mesh calculations. Next, we interpolate the band structure along paths originating from the Γ -point to map the entire spherical space. By integrating over the angular variables, our tool produces a 2D representation of the energy dispersion of electronic bands on spherical paths.

Suppl. Note 2. Methodology validation

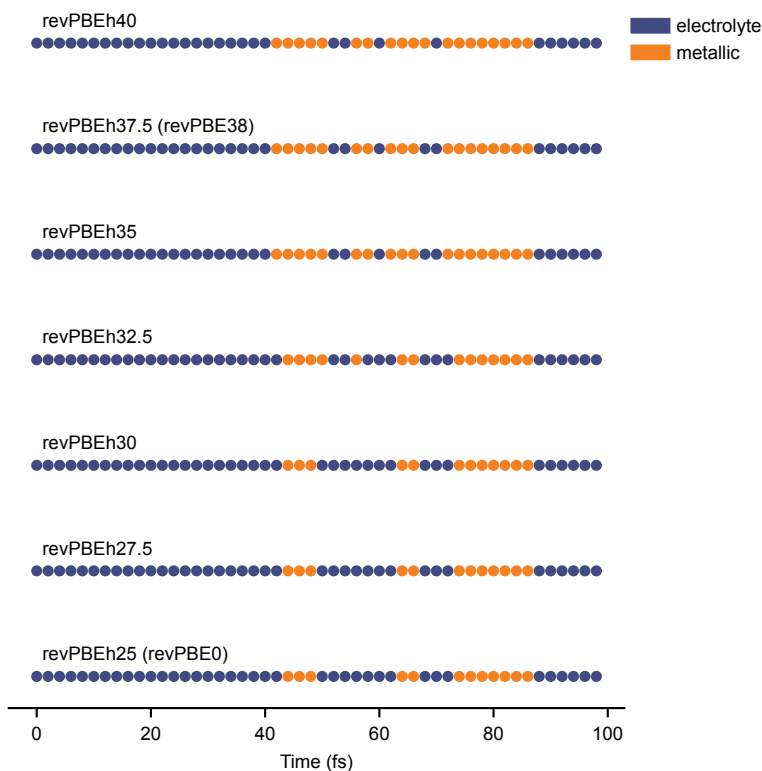
The primary computational work in this study is conducted using the revPBE38-D3 functional, applied for both AIMD trajectory propagation and subsequent electronic structure calculations. As demonstrated in the following sections, we assess that the revPBE38-D3 functional provides reliable results by examining its ability to capture the flipping behaviour between the metallic and electrolyte states and its close alignment with the electronic structure results obtained from the state-of-the-art G_0W_0 method.

Suppl. Note 2.1 Choice of density functional

To assess the robustness of our electronic structure results, we first propagated a trajectory for 10 ps using the revPBE0-D3 functional with a regular Nose-Hoover thermostat [35, 36] (time constant of 500 fs) and collected 50 snapshots at 2-fs intervals. We then performed electronic structure calculations on these snapshots using a $2 \times 2 \times 2$ k-point grid, employing various percentages of Hartree-Fock (HF) exchange within a revPBEh hybrid functional framework. The band gap and electronic mobility analysis determined whether each snapshot exhibited metallic or electrolyte behaviour.

Figure 1 shows the evolution of metallic and electrolyte states along the trajectory for revPBEh functionals with HF exchange percentages ranging from 25% to 40%. Interestingly, the results reveal that higher HF exchange percentages correlate with a greater occurrence of metallic states. This outcome is somewhat counterintuitive, as one would typically expect that increasing the HF exchange fraction would stabilize localized, non-metallic behaviour, thereby reducing metallic character.

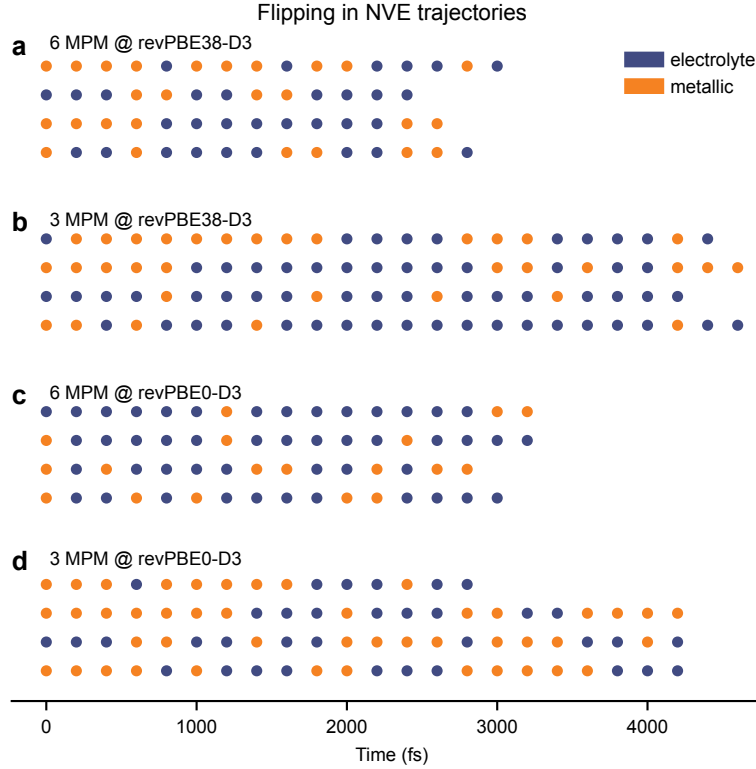
A possible explanation for this behaviour is that the underlying snapshots were propagated using the revPBE0-D3 functional with 25% HF exchange. Consequently, while the flipping behaviour remains present across different HF percentages, the frequency and stability of the metallic state appear to be influenced both by the HF exchange content of the functional used in the electronic structure calculations and the functional used during the initial trajectory propagation. This highlights the sensitivity of the electronic properties of the system to both the HF exchange level and the choice of functional during molecular dynamics.



Supplementary Figure 1. Distribution of metallic (orange) and electrolyte (blue) states across 50 snapshots taken at 2-fs intervals from a trajectory propagated with the revPBE0-D3 functional. Snapshots were analysed with varying HF exchange percentages (25% to 40%) to assess electronic structure changes associated with each functional.

To investigate the influence of the functional on the transition dynamics between metallic and electrolyte-like states, we conducted simulations at two different concentrations, 3.0 MPM and 6.0 MPM. For each concentration, we ran four NVE (microcanonical) ensemble trajectories using both revPBE0-D3 and revPBE38-D3 functionals. The use of NVE dynamics excludes any possible influence that the thermostat might have on the flipping behaviour. Snapshots were taken every 200 fs and electronic structure calculations were performed on a $2 \times 2 \times 2$ k-point grid using the same functional as used for propagating the trajectories. We determined whether each snapshot exhibited metallic or electrolyte behaviour based on band gap and electronic mobility analysis.

Figure 2 shows that, regardless of the functional used for the trajectory propagation, the system consistently flips between metallic and electrolyte states in all trajectories.



Supplementary Figure 2. Temporal fluctuations between metallic (orange) and electrolyte (blue) states for 3.0 MPM and 6.0 MPM concentrations in the microcanonical ensemble. Panels (a) and (b) show results for 6.0 MPM and 3.0 MPM, respectively, using the revPBE38-D3 functional. Panels (c) and (d) show results for 6.0 MPM and 3.0 MPM, respectively, using the revPBE0-D3 functional.

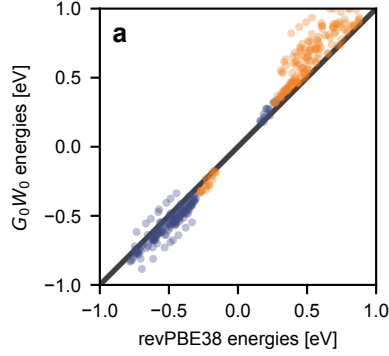
Combining results from Figures 1 and 2, we conclude that the flipping between metallic and electrolyte states is an intrinsic characteristic of the system, rather than an artifact of the thermostat or the choice of functional. While the transitions occur regardless of whether the revPBE0-D3 or revPBE38-D3 functional is used, what varies is the frequency of these transitions. Given the relatively small sampling windows used, however, we are cautious not to overinterpret these results.

In the following, we compare the calculated data using the revPBE38-D3 hybrid functional with the G_0W_0 method. Figures 3, 4, and 5 depict the correlation of the orbital energies (on a $2 \times 2 \times 2$ k-point mesh), the band gap energies (on a $2 \times 2 \times 2$ k-point mesh), and the charge carrier mobilities, respectively, for the 3.0 MPM system evaluated on 22 snapshots taken at 200-fs intervals.

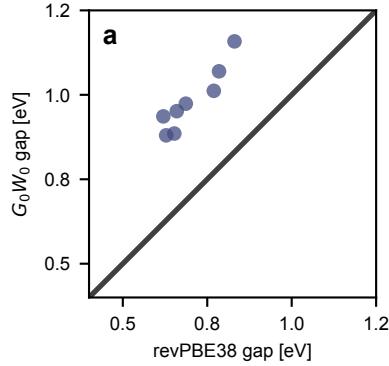
The reason for the choice of revPBE38-D3 functional is twofold:

1. A strong correlation between the two methods is evident across all selected snapshots. This is clearly demonstrated by the comparison of the simulation data in Figures 28, 29, and 30 with the black line, which represents $y=x$. This result is also in very good agreement with recent findings^[21] that state-of-the-art hybrid functionals provide very similar results to GW .
2. Using the G_0W_0 method for 2000 geometries becomes computationally prohibitive. On average, a single G_0W_0 calculation for one snapshot on $2 \times 2 \times 2$ k-point mesh requires approximately 3200 CPU hours on a 2×32 -CPU

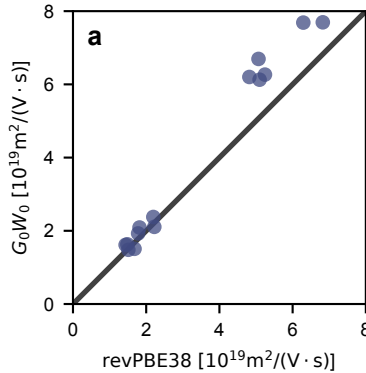
AMD EPYC 7543 @ 2.8 GHz node and demands around 800 GB of RAM due to the memory-intensive nature of GW method.



Supplementary Figure 3. Correlation of G_0W_0 versus revPBE38-D3 orbital energies on a $2 \times 2 \times 2$ k-point mesh for both 3.0 MPM system, considering only the valence band and conduction band. The black line represents $y = x$, highlighting the strong correlation between the data sets.



Supplementary Figure 4. Correlation of G_0W_0 versus revPBE38-D3 band gap energies on a $2 \times 2 \times 2$ k-point mesh for 3.0 system. AIMD snapshots with no band gap were excluded from the analysis. The black line represents $y = x$, highlighting the strong correlation between the data sets.

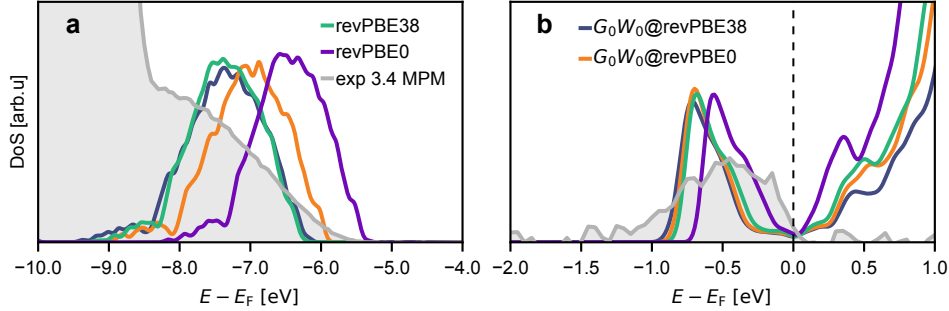


Supplementary Figure 5. Correlation of G_0W_0 versus revPBE38-D3 charge carrier mobilities for 3.0 MPM system. The black line represents $y = x$, highlighting the strong correlation between the data sets.

In Figure 6, we present the density of states (DoS) calculated using four different methods: revPBE38-D3 (green), revPBE0-D3 (purple), G_0W_0 @revPBE38-D3 (blue), and G_0W_0 @revPBE0-D3 (orange). Panel (a) illustrates the DoS in the energy range from -10 to -4 eV, while panel (b) focuses on the region near the Fermi level, from -2 to 1 eV.

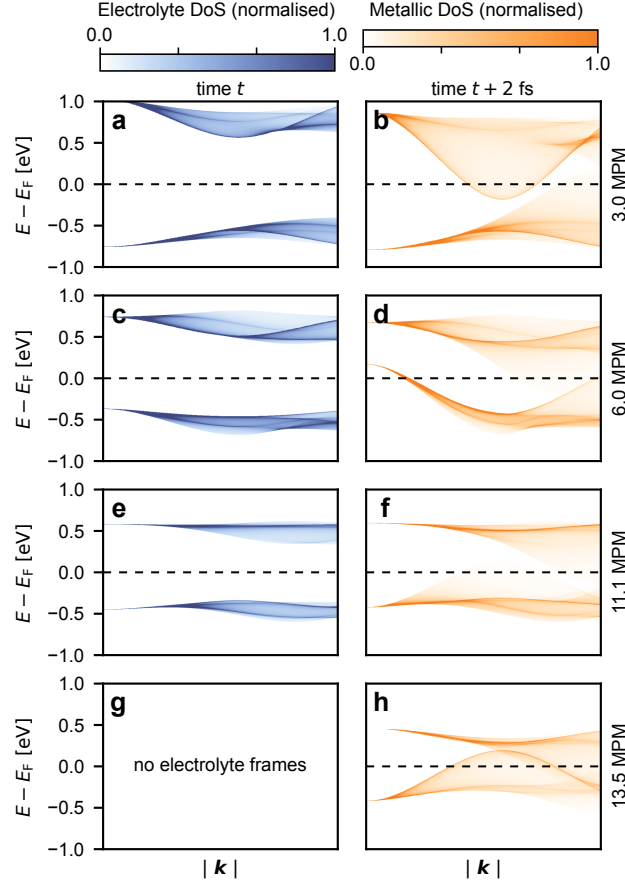
It is evident from both panels that the DoS obtained using G_0W_0 @revPBE38-D3 and revPBE38-D3 are nearly indistinguishable, indicating that the G_0W_0 @revPBE38-D3 method does not significantly alter the electronic structure compared to the revPBE38-D3 hybrid functional. This similarity supports the choice of revPBE38-D3 for our simulations, as it yields results consistent with many-body perturbation theory calculations while being computationally less expensive.

Furthermore, the calculated DoS curves fit well the experimental data (grey) measured at 3.4 MPM. The onset of the experimental peak in panel (a) is attributed to the $3a_1$ peak of liquid-phase ammonia, which is consistent with our simulation results. The rest of the experimental spectral features correspond to gas-phase ammonia; however, we have not deconvoluted these contributions. Therefore, we focus on the alignment of our simulated spectra with the onset of the experimental peak corresponding to the liquid phase.



Supplementary Figure 6. Comparison of the Density of States (DoS) using revPBE38-D3 (green), revPBE0-D3 (purple), G_0W_0 @revPBE38-D3 (blue), and G_0W_0 @revPBE0-D3 (orange) methods. Panel (a) shows the DoS near the valence band region, highlighting the close agreement between G_0W_0 @revPBE38-D3 and revPBE38-D3 and their match with the onset of the liquid-phase ammonia experimental peak measured at 3.4 MPM (grey). Panel (b) illustrates the DoS around the Fermi level. The experimental data were obtained from Ref. [28].

To further examine the impact of the G_0W_0 @revPBE38-D3 method on the temporal dynamics of the electrolyte-to-metal transition (EMT), we generated SBSs for two consecutive snapshots separated by 2 fs around the flipping event. These snapshots are identical to those used in Figure 4 of the main text, ensuring a direct comparison of the results obtained with different electronic structure methods. As shown in Figure 7, the resulting band structure closely resembles that obtained with the revPBE38-D3 functional described in the main text (Figure 4). This similarity underscores that the observed temporal fluctuations in the band gap and the switch between metallic and electrolyte behaviour are intrinsic to the system and not highly dependent on the choice of the method.



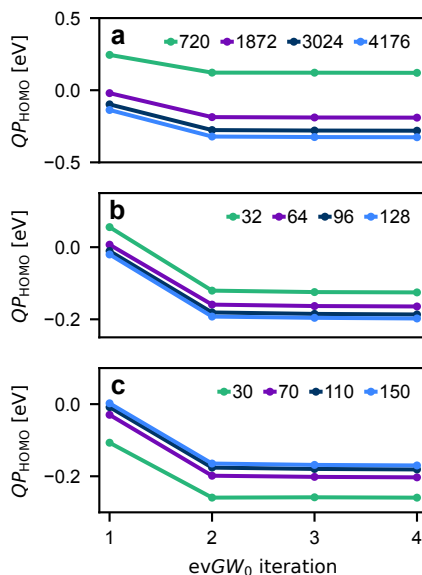
Supplementary Figure 7. SBS of consecutive electrolyte (a,c,e,g) and metallic (b,d,f,h) frames at 3.0, 6.0, 11.1 and 13.5 MPM calculated with G_0W_0 @revPBE38-D3. These G_0W_0 calculations were performed on identical snapshots, starting from the revPBE38-D3 results shown in Figure 4 of the main text. For clarity, only the valence and conduction bands near the Fermi level (black dashed line), E_F , are displayed. The SBS data are normalised such that the maximum displayed value is 1, with values exceeding 1 set to 1 to enhance contrast, consistently across all panels.

Suppl. Note 2.2 GW convergence

To ensure that our G_0W_0 results are reliable, we present key convergence benchmarks here.

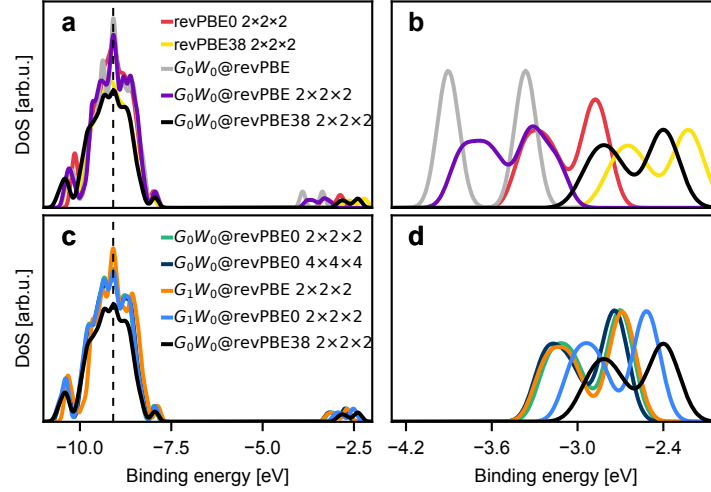
Many-Body Perturbation Theory calculations (MBPT) including GW , random-phase approximation (RPA), and Bethe-Salpeter equations (BSE), rely on sums over (unoccupied) states, and therefore require a large number of virtual (unoccupied) orbitals to converge. MBPT relies on the inclusion of these virtual orbitals to ensure accurate results, making the convergence of calculations with a large number of empty states very slow. Additionally, the quality and scaling of these calculations depend on several parameters:

1. The energy cutoff for the response function determines the maximum energy up to which plane waves are included, with higher cutoffs leading to more accurate but computationally intensive results.
2. The (imaginary) frequency and imaginary time grid points are crucial for the numerical evaluation of the frequency-dependent dielectric function and self-energy in GW calculations, impacting both accuracy and efficiency.
3. Gaussian smearing is employed to smooth the electronic density of states (DoS) and facilitate convergence. An optimal smearing value of 0.075 eV maintains sharp spectral features while avoiding artificial broadening or artefacts in the DoS.



Supplementary Figure 8. $evGW_0$ HOMO quasi-particle energies with respect to the total number of Kohn-Sham orbitals (a), energy cutoff for the response function (b), and (imaginary) frequency and imaginary time grid points (c). All calculations were performed at the Γ -point only.

In Figure 8a, the energy cutoff for the response function was set to 50 eV, and the (imaginary) frequency and imaginary time grid points were set to 80. In Figure 8b, the total number of Kohn-Sham orbitals was set to 2160, and the (imaginary) frequency and imaginary time grid points were set to 80. In Figure 8c, the total number of Kohn-Sham orbitals was set to 2160, and the energy cutoff for the response function was set to 120 eV.



Supplementary Figure 9. Density of States (DoS) calculations with various methods and k -point grids. Panel (a) compares the DoS obtained using four different methods, revPBE0-D3 (red), revPBE38-D3 (yellow), G_0W_0 @revPBE-D3 at the gamma point (grey), G_0W_0 @revPBE-D3 on a $2 \times 2 \times 2$ k -point grid (purple), and G_0W_0 @revPBE38-D3 on a $2 \times 2 \times 2$ k -point grid (black). Panels (b,d) provide an enlarged view of the peak region for solvated electrons using the same calculation methods. Panel (c) compares the DoS using G_0W_0 @revPBE0-D3 on $2 \times 2 \times 2$ (green) and $4 \times 4 \times 4$ (dark blue) k -point grids, G_1W_0 @revPBE-D3 on a $2 \times 2 \times 2$ k -point grid (orange), G_1W_0 @revPBE0-D3 on a $2 \times 2 \times 2$ k -point grid (blue) and G_0W_0 @revPBE38-D3 on a $2 \times 2 \times 2$ k -point grid (black). The vertical dashed line represents the experimental value of the $3a_1$ valence orbital of ammonia peaking at -9.09 eV.

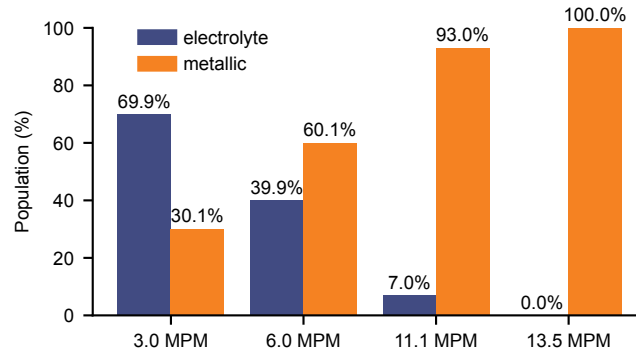
Using a larger k -point grid is computationally prohibitive due to the significant cost associated with such calculations. To address this limitation, we employed high-level G_0W_0 calculations to accurately determine quasiparticle band energies. Figure 9 illustrates the DoS calculations using various methods and k -point grids. The vertical dashed line represents the experimental value of the $3a_1$ valence orbital of ammonia peaking at -9.09 eV [37]. Experimentally, the peaks of solvated electrons and dielectrons are observed between -1.5 to -2.5 eV binding energy [28] and the objective was to find a computational method that closely matches these experimental peaks while remaining computationally feasible.

For all GW calculations, the energy cutoff for the response function was set to 100 eV, the (imaginary) frequency and imaginary time grid points were set to 100, the total number of Kohn-Sham orbitals was set to 2240, and Gaussian smearing was set to 0.075 eV. We selected G_0W_0 @revPBE38-D3 on a $2 \times 2 \times 2$ k -point mesh as the best choice to validate our revPBE38-D3 data in the main text, given its optimal balance of accuracy and computational efficiency.

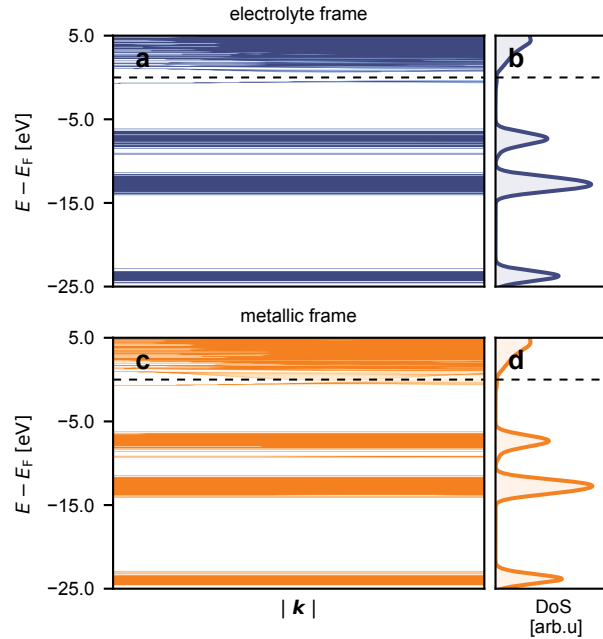
Suppl. Note 3. Extended data analysis

This section provides an extended analysis to complement the main findings on concentration-dependent transition dynamics. By examining the population of metallic and electrolyte states across various concentrations, we gain deeper insights into how increased concentration shifts the system's electronic character.

To provide additional context to the transition dynamics described in Figure 2 of the main text, we present the percentage-based population of metallic and electrolyte states at concentrations of 3.0, 6.0, 11.1, and 13.5 MPM (Figure 10). As shown in the bar chart, the system undergoes a clear concentration-dependent shift from predominantly electrolyte to metallic behaviour. At 3.0 MPM, 69.9% of the states are electrolyte, with 30.1% metallic. At 6.0 MPM, metallic states increase to 60.1%, while electrolyte states decrease to 39.9%. At 11.1 MPM, the system becomes predominantly metallic, with 93.0% of the states metallic and only 7.0% electrolyte. By 13.5 MPM, the system is entirely metallic at 100.0%. This trend supports the concentration-driven transition observed in Figure 2, highlighting how increased concentration leads to a more metallic character. The flip times and intervals are summarised in Table 1.



Supplementary Figure 10. Percentage-based population of metallic (orange) and electrolyte-like (blue) states at concentrations of 3.0, 6.0, 11.1, and 13.5 MPM.



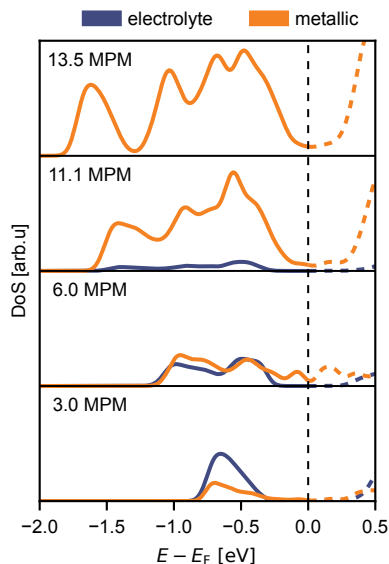
Supplementary Figure 11. Example of full SBS and corresponding DoS (excluding Li^+ peaks) evaluated by G_0W_0 starting from revPBE38-D3 wave function for 2 consecutive snapshots right after the flip event for 3.0 MPM system, electrolyte frame (a,b), metallic frame (c,d)

Figure 11 presents the full SBS and corresponding DoS for two consecutive snapshots following a flip event in the 3.0 MPM system, evaluated using G_0W_0 based on the revPBE38-D3 wave function. Panels (a) and (b) show the SBS and DoS for an electrolyte-like frame, while panels (c) and (d) display the corresponding data for a metallic frame. This comprehensive band structure visualization includes energy levels beyond the immediate vicinity of the Fermi level, providing a broader perspective on the system's electronic structure and highlighting the contrasting band distributions in the electrolyte and metallic states. The SBS and DoS excludes contributions from Li^+ peaks for clarity.

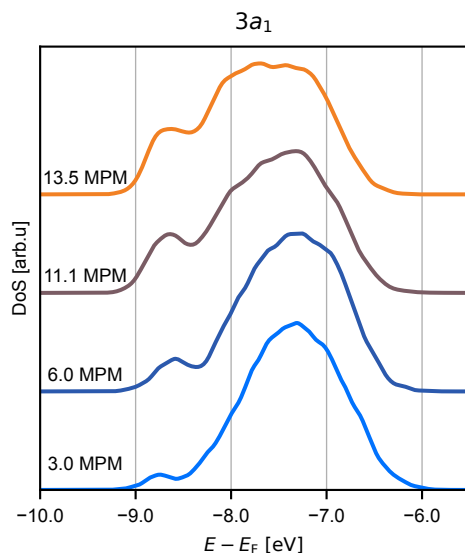
3.0 MPM		6.0 MPM		11.0 MPM	
Flip Time (fs)	Interval (fs)	Flip Time (fs)	Interval (fs)	Flip Time (fs)	Interval (fs)
8.0	16.0	70.0	16.0	34.0	2.0
24.0	10.0	86.0	6.0	36.0	16.0
34.0	176.0	92.0	8.0	52.0	2.0
210.0	4.0	100.0	4.0	54.0	54.0
214.0	108.0	104.0	4.0	108.0	4.0
322.0	14.0	108.0	38.0	112.0	44.0
336.0	40.0	146.0	4.0	156.0	6.0
376.0	10.0	150.0	2.0	162.0	2.0
386.0	64.0	152.0	6.0	164.0	2.0
450.0	10.0	158.0	16.0	166.0	12.0
460.0	2.0	174.0	2.0	178.0	2.0
462.0	6.0	176.0	50.0	180.0	4.0
468.0	4.0	226.0	8.0	184.0	10.0
472.0	36.0	234.0	2.0	194.0	2.0
508.0	2.0	236.0	2.0	196.0	4.0
510.0	18.0	238.0	98.0	200.0	68.0
528.0	10.0	336.0	10.0	268.0	18.0
538.0	14.0	346.0	16.0	286.0	346.0
552.0	26.0	362.0	20.0	632.0	20.0
578.0	4.0	382.0	8.0	652.0	—
582.0	80.0	390.0	98.0	—	—
662.0	54.0	488.0	2.0	—	—
716.0	4.0	490.0	110.0	—	—
720.0	70.0	600.0	8.0	—	—
790.0	6.0	608.0	2.0	—	—
796.0	14.0	610.0	20.0	—	—
810.0	26.0	630.0	2.0	—	—
836.0	2.0	632.0	2.0	—	—
838.0	4.0	634.0	4.0	—	—
842.0	2.0	638.0	50.0	—	—
844.0	100.0	688.0	14.0	—	—
944.0	22.0	702.0	4.0	—	—
966.0	18.0	706.0	8.0	—	—
984.0	4.0	714.0	12.0	—	—
988.0	—	726.0	14.0	—	—
—	—	740.0	114.0	—	—
—	—	854.0	20.0	—	—
—	—	874.0	6.0	—	—
—	—	880.0	34.0	—	—
—	—	914.0	2.0	—	—
—	—	916.0	14.0	—	—
—	—	930.0	—	—	—
Statistics		3.0 MPM	6.0 MPM	11.0 MPM	
Number of flips		35	42	20	
Mean interval (fs)		28.8	21.0	32.5	
Median interval (fs)		14.0	8.0	6.0	
Standard deviation (fs)		38.3	30.1	76.2	
Standard error (fs)		6.6	4.8	18.0	
Time in metallic state (fs)		302.0	600.0	930.0	
Time in electrolyte state (fs)		698.0	400.0	70.0	

Supplementary Table 1. Consolidated flip analysis summary for the time evolution of DoS at 3.0, 6.0, and 11.0 MPM concentrations. The table presents the flip times between metallic and electrolyte states and the intervals between flips.

Figure 12 presents the DoS calculated using the revPBE38-D3 functional, separated into contributions from metallic (orange) and electrolyte (blue) states for concentrations of 3.0, 6.0, 11.1, and 13.5 MPM. At 3.0 MPM, electrolyte states dominate the DoS, with metallic states contributing only minimally. As the concentration increases, the metallic contribution becomes more pronounced, eventually surpassing the electrolyte contribution at higher concentrations. By 11.1 MPM and 13.5 MPM, the DoS is predominantly metallic, consistent with the system exhibiting a metallic character.



Supplementary Figure 12. DoS calculated using the revPBE38-D3 functional, split into metallic (orange) and electrolyte (blue) states across concentrations of 3.0, 6.0, 11.1, and 13.5 MPM. The dashed line indicates the Fermi level (E_F)

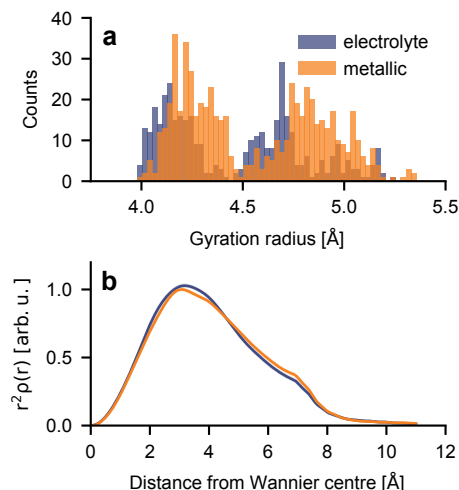


Supplementary Figure 13. DoS for revPBE38-D3 calculations at various concentrations (3.0 to 13.5 MPM). The figure focuses on the $3a_1$ peak, which broadens progressively with increasing concentration, consistent with experimental photoelectron spectroscopy data reported in reference [28].

Figure 13 illustrates the DoS calculated using revPBE38-D3 for various concentrations, focusing on the $3a_1$ peak. As the concentration increases, the $3a_1$ peak exhibits noticeable broadening, particularly at higher concentrations. This trend aligns with experimental observations reported in reference [28], reflecting the increasing metallic character of the system.

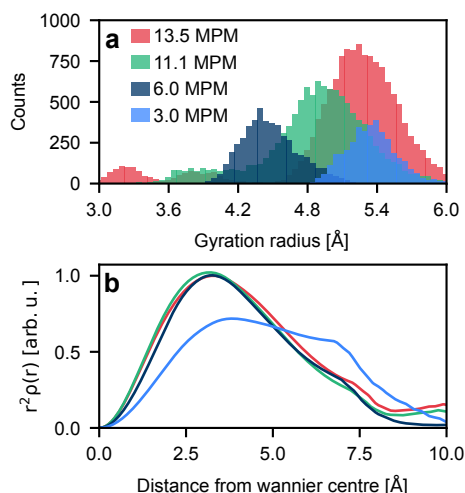
Figure 14 provides an analysis of the spatial extent and density distribution of solvated dielectrons at 6.0 MPM, obtained using the revPBE38-D3 functional. Panel a illustrates the gyration radii distributions for metallic (orange) and electrolyte (blue) states. Panel b presents the radial distribution profiles of excess electron density, centred on the Wannier orbitals, averaged separately for metallic and electrolyte states.

At 6.0 MPM, the system contains two dielectrons, and the overall state, whether metallic or electrolyte, is determined based on bandgap and conductivity criteria. However, it is not possible to correlate the state of the system to individual



Supplementary Figure 14. Analysis of solvated dielectron density and volumetric properties in the 6.0 MPM alkali metal-ammonia solution obtained with the revPBE38-D3 functional. Panel (a) shows the distribution of gyration radii for metallic (orange) and electrolyte (blue) states. Panel (b) presents the radial distribution profiles of excess electron density from the Wannier centre, averaged separately for metallic and electrolyte states.

gyration radii, as the metallic or electrolyte behaviour is a property of the system as a whole. Both dielectrons contribute to the overall state simultaneously, and while one dielectron may be more localized (smaller gyration radius) and the other more delocalized (larger gyration radius), their combined behaviour determines whether the system exhibits metallic or electrolyte characteristics. Both panels reveal that when using the revPBE38-D3 functional, the spatial extents of the metallic and electrolyte states are similar at 6.0 MPM, with no significant differences observed in the gyration radii distributions. However, when using the revPBE0-D3 functional (see Section Suppl. Note 5.), a clear distinction between metallic and electrolyte states is more evident. This discrepancy may arise from the higher fraction of exact exchange in revPBE38-D3, which reduces the contrast between the two states at intermediate concentrations. However, given the relatively small sampling size used, we are cautious not to overinterpret these results.



Supplementary Figure 15. The analysis of structural properties of an alkali-metal ammonia solution across concentrations ranging from 3.0 – 13.5 MPM obtained with revPBE38-D3 functional. The top panel (a) illustrates the radii of gyration, while the bottom panel (b) provides the spherically integrated electron density profiles.

To examine the EMT transition in terms of the structure of the excess electron density, we analysed 3940, 2514, 2706 and 2794 snapshots sampled at 5-femtosecond intervals from the 3.0, 6.0, 11.1, and 13.5 MPM AIMD trajectories (Figure 15). The data reveal significant variations in the gyration radii of single dielectrons. At a concentration of

3.0 MPM, the gyration radius is around 5.3 Å. When the concentration is increased to 6.0 MPM (2 dielectrons), the dielectrons likely experience mutual repulsion or localisation effects due to counter ions, resulting in a reduced gyration radius of 4.5 Å.

As the concentration further increases, the gyration radii steadily rise to 4.9, and 5.1 Å at 11.1, and 13.5 MPM, respectively, indicating increased delocalisation with higher concentrations. However, small but non-negligible populations with gyration radii around 3.2 Å (for 13.5 MPM) and 3.8 Å (for 11.1 MPM) suggest structural inhomogeneities in the system at higher concentrations.

As the concentration of dielectrons increases, the gyration radius distributions reveal a complex interplay between electron delocalisation and confinement. At low concentrations, such as 3.0 MPM, a single dielectron has more freedom to delocalise, resulting in a relatively large gyration radius. When the concentration increases to 6.0 MPM, the presence of a second dielectron introduces mutual repulsion and stabilization by nearby Li^+ cations, leading to slightly more confined, smaller gyration radii. However, at higher concentrations (11.1, and 13.5 MPM), we observe a broadening in the gyration radius distribution, indicating a coexistence of both localized and delocalized electron states. This behaviour suggests that electron-electron repulsion drives some dielectrons to spread out more, leading to larger gyration radii, while interactions with additional Li^+ cations simultaneously stabilize other dielectrons in more confined configurations. At the highest concentrations (11.1 and 13.5 MPM), this results in a multimodal distribution, with distinct populations corresponding to localized and delocalized states. This distribution reflects a concentration-dependent transition, with the system exhibiting both metallic and electrolyte behaviours as different dielectrons experience varying degrees of spatial confinement. Overall, the structure of the excess electrons is complex and varies significantly with concentration.

Suppl. Note 4. Experimental photoelectron spectra and fitting procedures

In the following, we summarise the data analysis and the fitting model, which were described in detail in the main text and the supplementary information of reference [28]. Figure 16 depicts the measured photoelectron (PE) spectra for lithium in liquid ammonia at four concentrations (bottom to top panels): 0.35, 0.97, 3.4, and 9.7 MPM.

At 0.35 MPM, the PE spectrum reveals only a symmetric spectral feature corresponding to solvated di-electrons, consistent with theoretical modelling described in reference [28]. At the highest concentration (9.7 MPM), three distinct spectral features are observed. A comparison with another liquid metal, the sodium-potassium (NaK) alloy, allowed us to assign the asymmetric spectral feature at the lowest binding energy to the conduction band and its Fermi level, while the other two features correspond to bulk plasmons.

At the time of the original study, no simulation framework capable of handling higher concentrations of excess electrons was available. Therefore, the free electron gas model (FEM), a solid-state theory, was employed. FEM assumes that, apart from boundary conditions, the interaction between cationic atomic species and valence electrons can largely be neglected. Importantly, FEM does not rely on any assumptions regarding periodic structures, making it applicable to disordered or amorphous condensed matter systems.

In FEM, two key experimental parameters influence the binding energy positions and widths of spectral features: the excess electron density and the reduced mass of the electrons. While the excess electron density is determined by the amount of dissolved lithium in the liquid ammonia solutions, the reduced mass was used as the sole fitting parameter.

Based on this approach, a fit function was designed that incorporates FEM features while also accounting for spectral intensity at the energetic position of the solvated di-electron. This fitting procedure is physically justified by treating the localised solvated di-electrons as representative of the electrolyte-like character of the solution, while the spectral signatures of the conduction band and plasmons represent delocalised electrons indicative of metallic behaviour. Furthermore, the electronic structure was assumed to be an additive mixture of solvated di-electrons coexisting with free electrons forming the conduction band.

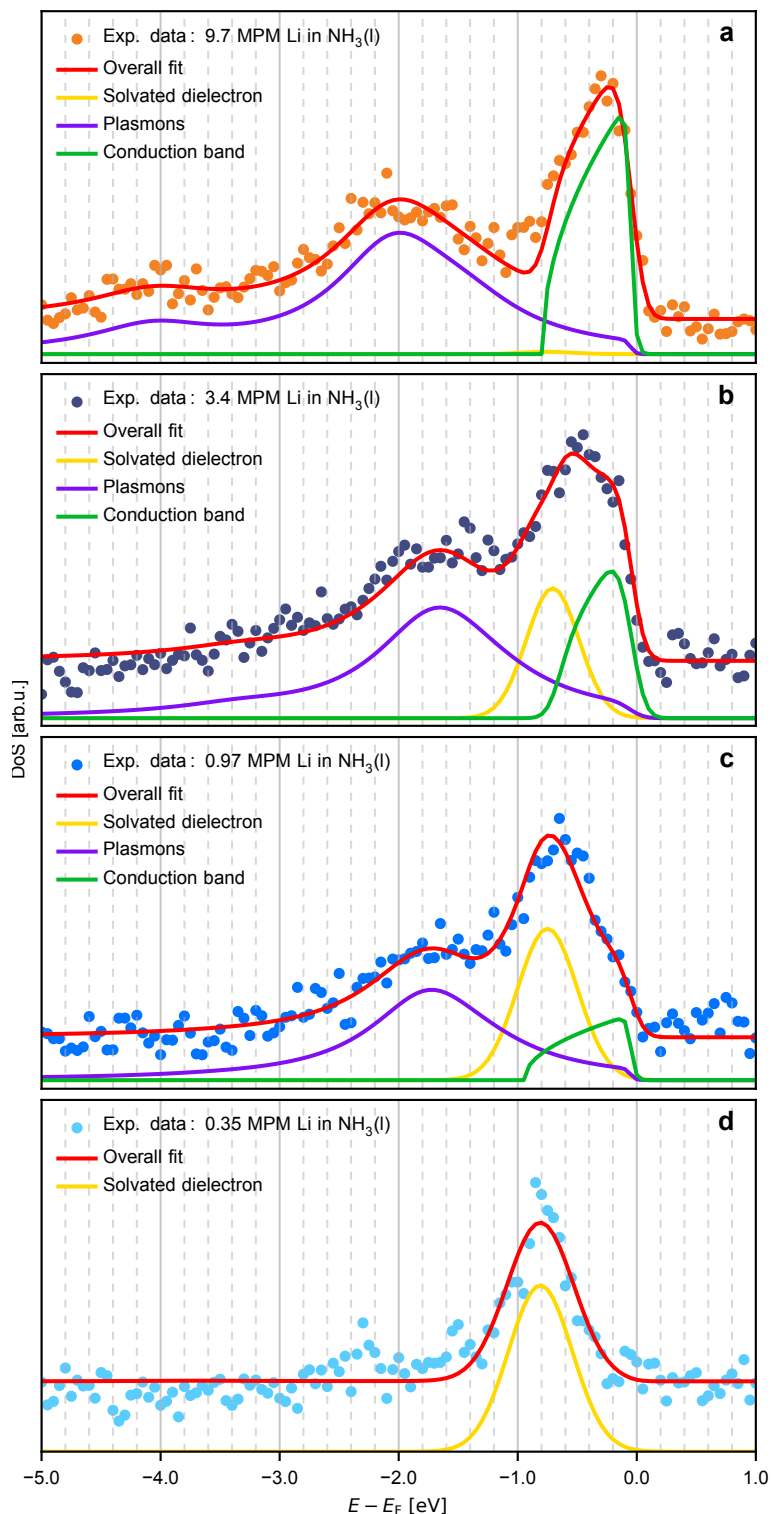
Figure 16 illustrates the overall fit to the experimental data (red line) compared to the measured data (dots). The design of the fit function allows for a decomposition of the PE spectral intensity into contributions from the solvated di-electrons (yellow line), the conduction band (green line), and the plasmon (purple line), enabling quantification of the localised and delocalised electronic components.

Moreover, this fitting procedure allows for estimation of confidence intervals by calculating relative root mean square deviations (RSM) between the fits and the (scattered) experimental data, as done in reference [28]. The shaded regions in all panels of Figure 5 in the main text represent the RSM of the experimental data fits, computed as the root mean square of the difference between the experimental photoelectron (PE) spectra and the fitted model.

Suppl. Note 4.1 Comparison of calculated DoS versus measured PE spectra

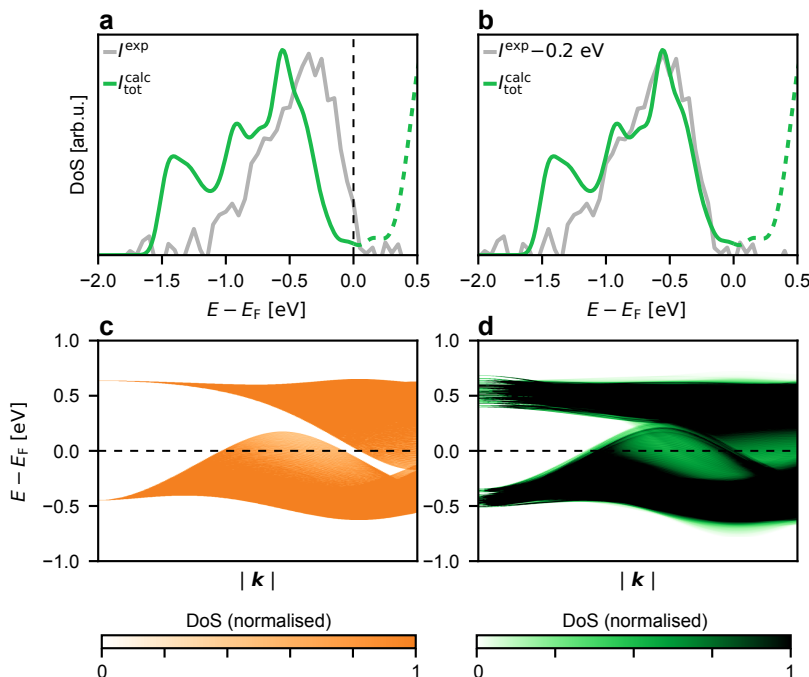
In this section, we expand on the comparison between the measured photoemission spectra and the calculated DoS. Figure 17a reproduces the plot shown in Figure 5a of the main text, comparing the DoS calculated for a lithium-ammonia solution at 11.1 MPM with the experimental photoelectron (PE) spectra measured at 9.7 MPM. In the main text, we noted that the simulated DoS reveals a subtle pre-edge feature near the Fermi level, contributing approximately 5 % to the total spectral intensity. To further investigate this feature, we plotted the same data in Figure 17b, shifting the experimental PE spectrum by -0.2 eV to align with the main slope of the calculated DoS. The resulting alignment demonstrates excellent agreement in terms of the shape and width of the conduction band. However, the average noise level in the experiment — approximately 10 % of the highest signal intensity — is too high to resolve such small features. Recent experimental advancements, however, allow for the determination of the Fermi level's energetic position, irrespective of whether the solution is metallic or electrolyte-like [37–40]. Thus, we are currently preparing to re-measure these alkali metal-ammonia solutions under improved experimental conditions.

To examine the DoS at the Fermi level in greater detail — particularly the pre-edge feature — we inspect the SBS of the 11.1 MPM system. First we look at the SBS from a single AIMD snapshot plotted in Figure 17c (with enhanced contrast compared to Figure 7f). The overlap between the conduction and valence band is minimal, occurring only at high $|\mathbf{k}|$ near the edge of the first Brillouin zone. This indicates that only a small fraction of valence band electrons can delocalise into the conduction band. In contrast, the fully metallic 13.5 MPM solution (Figure 7h and Figure 1k in the main text) exhibits a significantly larger overlap between the conduction and valence band. Figure 17d depicts the SBS summed up over 1 ps, showing a much larger overlap between conduction and valence band. However, this time averaged result might be misleading, as the band crossing is seldom established at any point in time. A more detailed



Supplementary Figure 16. Photoelectron spectra of lithium-ammonia solutions at concentrations of 9.7 MPM (a), 3.4 MPM (b), 0.97 MPM (c), and 0.35 MPM (d). Experimental data are shown as dots, while the red line represents the overall fit. Individual spectral contributions include the solvated dielectron peak (yellow line), the conduction band (green line), and the plasmons (purple line). The experimental data were obtained from Ref. [28].

analysis of individual SBSs would be necessary to fully resolve this issue, but such an investigation is beyond the scope of the current study.

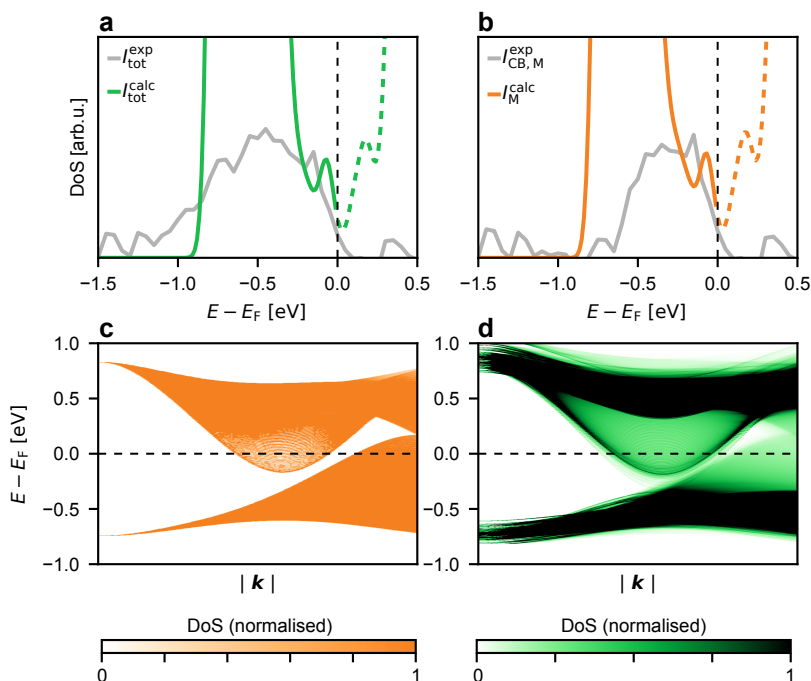


Supplementary Figure 17. Density of states (DoS) comparison for alkali metal-ammonia solutions at 11.1 MPM concentration using revPBE38-D3 calculations and experimental photoelectron (PE) spectra measured at 9.7 MPM. (a) Total calculated DoS (green) compared with the total experimental PE spectra (grey). (b) Total calculated DoS (green) compared with the total experimental PE spectra (grey) shifted by -0.2 eV. (c) SBS of single metallic AIMD snapshot at 11.1 MPM. (d) SBS time averaged over a 1 ps segment of AIMD at 11.1 MPM. The dashed line indicates the Fermi level (E_F). The experimental data were obtained from Ref. [28]. The SBS data are normalised such that the maximum displayed value is 1, with values exceeding 1 set to 1 to enhance contrast.

Figure 18 compares the calculated DoS for lithium-ammonia solutions at 3.0 MPM (obtained using the revPBE38-D3 functional) with experimental photoelectron (PE) spectra measured at 3.4 MPM. In Figure 18a, the total calculated DoS (green) is compared with the total experimental PE spectra (grey) as measured. Panel b focuses on the metallic components of the calculated DoS (orange) and compares them to the part of the experimental PE spectra corresponding to the conduction band (grey), which was decomposed using the fitting procedure described earlier. The dashed line indicates the Fermi level (E_F).

While neither the total DoS nor the decomposed metallic DoS components align perfectly with the experimental spectra, both reveal similar trends. The simulated DoS exhibits a small but non-zero intensity near the Fermi level (in the range -0.2 to 0.0 eV), indicative of partially delocalised states. The majority of the simulated DoS intensity, however, is concentrated in the range -0.9 to -0.2 eV, corresponding to the spectral region where solvated di-electrons are expected.

Examining a single SBS of the metallic frames in Figure 18c (also shown in Figure 7b) strongly indicates a semimetallic character of the solution at this concentration. The valence and conduction band show minimal overlap, with only slight contact at high $|\mathbf{k}|$ near the edge of the first Brillouin zone. Similarly, the time averaged SBS shown in Figure 18d exhibits very limited overlap between the valence and conduction band. It remains speculative, and more dedicated calculations are needed to investigate the semimetallic character in greater detail. Furthermore, experimental angular-resolved photoelectron investigations do not appear feasible for liquid jets of alkali-metal ammonia solutions.



Supplementary Figure 18. Density of states (DoS) comparison for alkali metal-ammonia solutions at 3.0 MPM concentration using revPBE38-D3 calculations and experimental photoelectron (PE) spectra measured at 3.4 MPM. (a) Total calculated DoS (green) compared with the total experimental PE spectra (grey). (b) Metallic components of the calculated DoS (orange) compared with experimental PE spectra of the conduction band (grey). (c) SBS of a single metallic AIMD snapshot at 3.0 MPM. (d) SBS time averaged over a 1 ps segment of AIMD at 3.0 MPM. The dashed line indicates the Fermi level (E_F). The experimental data were obtained from Ref. [28]. The SBS data are normalised such that the maximum displayed value is 1, with values exceeding 1 set to 1 to enhance contrast.

Suppl. Note 5. Supplementary data and analysis — revPBE0-D3 trajectories

In this supplementary analysis, we examine simulations that differ from the main study in both functional and thermostat choice, offering a broader perspective on the electronic structure behaviour of solvated dielectron systems. Specifically, we present results from revPBE0-D3 trajectories run with the Nose–Hoover thermostat, supplemented by G_0W_0 electronic structure calculations based on revPBE0-D3, which yield analogous but quantitatively slightly different results.

We investigated systems composed of 64 ammonia molecules with varying concentrations of solvated dielectrons and Li^+ cations under periodic boundary conditions: 3.0 MPM, corresponding to 1 dielectron (2 Li^+) within a 14.241 Å box; 6.0 MPM, with 2 dielectrons (4 Li^+) in a 14.486 Å box; 8.5 MPM, with 3 dielectrons (6 Li^+) in a 14.730 Å box; 11.1 MPM, with 4 dielectrons (8 Li^+) in a 14.975 Å box; and 13.5 MPM, with 5 dielectrons (10 Li^+) in a 15.218 Å box. These target volumes were estimated from the experimental density of liquid lithium ammonia solutions [1].

Following initial force-field molecular dynamics (FFMD) equilibration, where bromine anions served as placeholders for dielectron cavities (see section Suppl. Note 1.1), we ran four 5-nanosecond trajectories per system. For these additional AIMD simulations, we transitioned to ab initio molecular dynamics (AIMD) using the revPBE0-D3 functional and regular Nose–Hoover thermostat [35, 36], rather than the micro-canonical (NVE) ensemble used in the main study with revPBE38-D3 (see section Suppl. Note 1.2). Each system was equilibrated for approximately 2 ps, followed by a 5 ps production run per trajectory. The cumulative lengths of the production runs for the 3.0, 6.0, 8.5, 11.1, and 13.5 MPM systems were 20.87, 21.64, 20.79, 21.07, and 20.87 ps, respectively.

In addition to these trajectories, we performed electronic structure calculations to examine the impact of different functionals and methodologies. For 3.0, 6.0, and 11.1 MPM systems, 100 G_0W_0 calculations were performed on snapshots taken at 200-fs intervals (see section Suppl. Note 1.3), using revPBE0-D3 as the starting wave function.

To identify potential structural differences between metallic and electrolyte states in electron density distribution of individual dielectrons, we conducted 1000 revPBE0-D3 Density of States (DoS) calculations (section Suppl. Note 1.3) on a $2 \times 2 \times 2$ k -point mesh for the 3.0 MPM trajectory, taken at 20-femtosecond intervals.

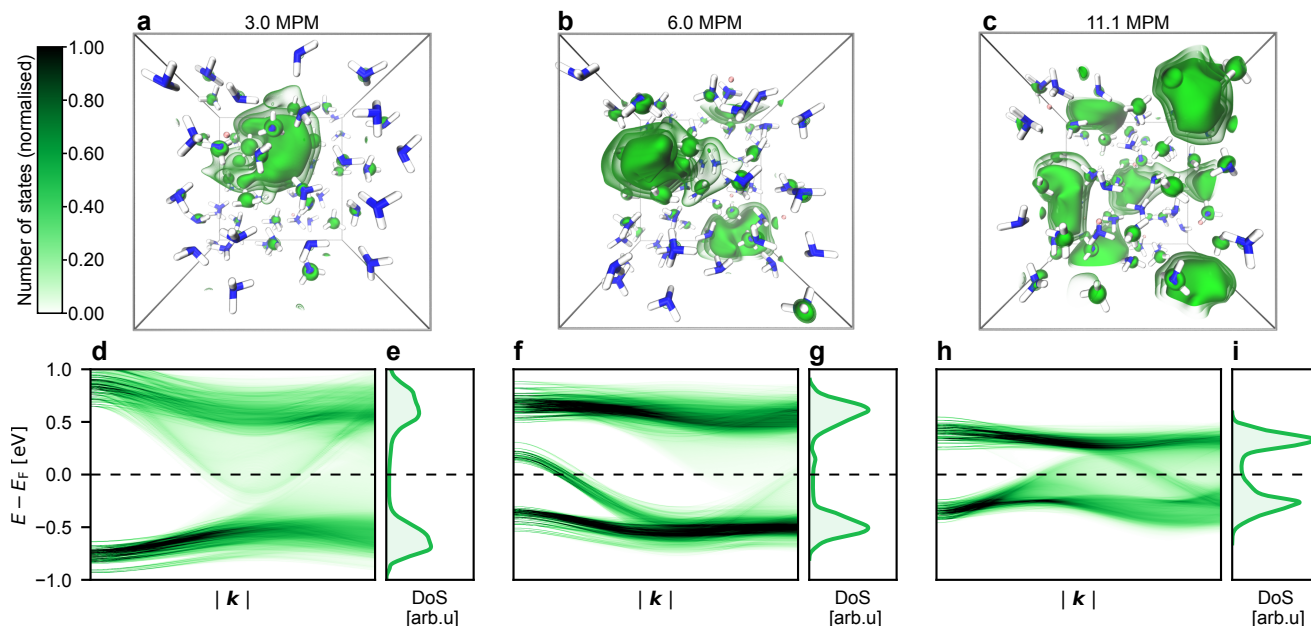
For the analysis of solvated electron density (see section Suppl. Note 1.5) distributions across the entire EMT range (3.0–13.5 MPM), we conducted 4176, 4330, 4159, 4218, and 4176 revPBE0-D3 gamma point calculations sampled at 5-femtosecond intervals from the 3.0, 6.0, 8.5, 11.1, and 13.5 MPM AIMD trajectories.

This extended analysis provides insights into how the system behaves under different functional choices (revPBE0-D3 vs. revPBE38-D3) and ensembles (NVT vs. NVE), offering a comparative view of the electrolyte-to-metal transition in solvated electrons in liquid ammonia.

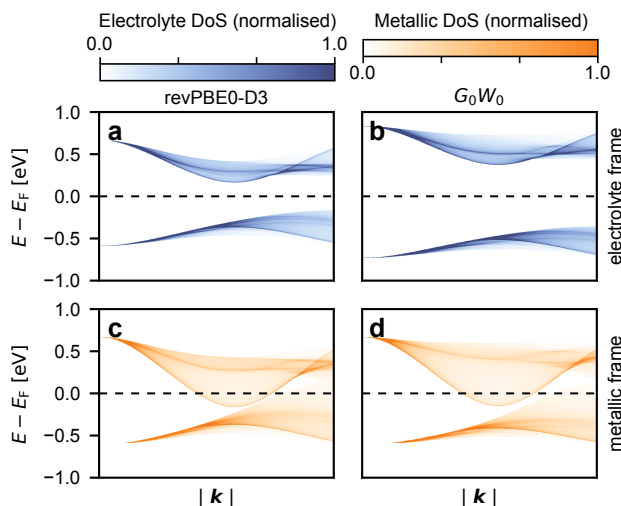
Suppl. Note 5.1 Spherical band structures

In Figure 19, we present spherical band structures (SBS) and density of states (DoS) computed from a set of 100 decorrelated snapshots taken at 200-fs intervals for alkali metal–ammonia solutions across the electrolyte-to-metal transition (EMT) concentration range. Unlike in the main text, where revPBE38-D3 was used for electronic structure calculations, here we employ the G_0W_0 method starting from revPBE0-D3 wave functions to achieve a higher level of accuracy. The results reveal a concentration-dependent transition, capturing the gradual narrowing and filling of the band gap as metallic behaviour emerges.

Figure 20 provides a benchmark comparison of spherical band structures (SBS) calculated with revPBE0-D3 and G_0W_0 for two consecutive snapshots immediately following a flip event in the 3.0 MPM system. The zoomed-in views around the Fermi level E_F (panels b and d) highlight the similarity in band structure features between the two methods, demonstrating consistent electronic behaviour in both electrolyte and metallic frames across different levels of theory.



Supplementary Figure 19. Representative AIMD simulation snapshots and corresponding electronic properties of alkali metal-ammonia solutions at various concentrations. The top panels show the simulation box for concentrations of a) 3.0 MPM, b) 6.0 MPM, and c) 11.1 MPM, illustrating the spatial distribution of solvated electrons within the solvent. The bottom panels display the corresponding SBS (d,f,h) and associated DoS (e,g,i) calculated by G_0W_0 method, starting from revPBE0-D3 wave function. For clarity, only the valence and conduction bands near the Fermi level (black dashed line), E_F , are displayed. The SBS data are normalised such that the maximum displayed value is 1, with values exceeding 1 set to 1 to enhance contrast, consistently across all panels.

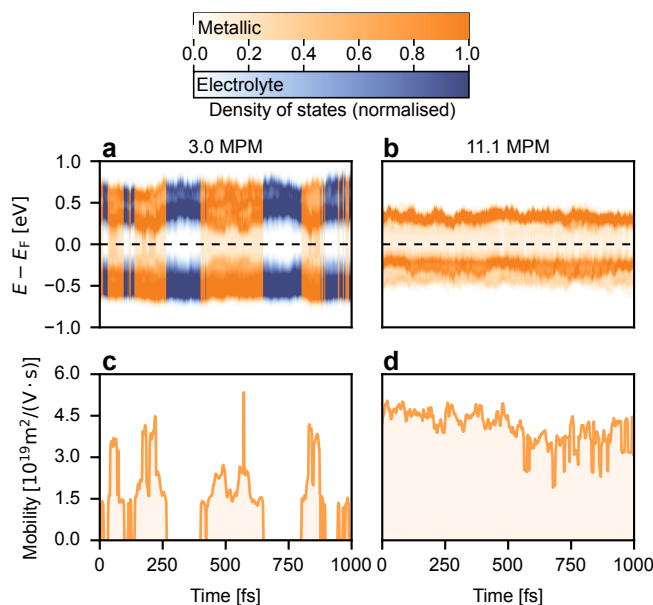


Supplementary Figure 20. The SBS evaluated by G_0W_0 and revPBE0-D3 for 2 consecutive snapshots right after the flip event for 3.0 MPM system. Panels (a) and (b) show the electrolyte frames obtained using revPBE0-D3 and G_0W_0 , respectively. Panels (c) and (d) display the corresponding metallic frames for revPBE0-D3 and G_0W_0 . For clarity, only the valence and conduction bands near the Fermi level (black dashed line), E_F , are displayed. The SBS data are normalised such that the maximum displayed value is 1, with values exceeding 1 set to 1 to enhance contrast, consistently across all panels.

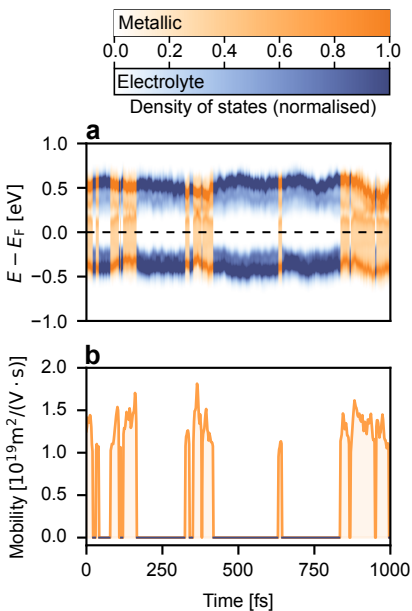
Suppl. Note 5.2 Fluctuations in DoS

The rapid fluctuations in the DoS, particularly at the Fermi level, and the charge carrier mobility were analysed using AIMD snapshots at 3.0, 6.0 MPM and 11.1 MPM concentrations, sampled every 2 fs (Figure 21 and Figure 22). Panels a and b of Figure 21 and panel a of Figure 22 show the band gap opening and closing over time, while panels c, d

of Figure 21 and panel b of Figure 22 illustrate the corresponding sharp changes in charge carrier mobility, which perfectly coincides with the band gap opening and closing. This interrelation characterises the fast transitions between the metallic and electrolyte states. As we discuss in more detail in the main manuscript, these rapid changes indicate a dynamic environment with significant temporal variability.



Supplementary Figure 21. Temporal evolution of the DoS (a, b) and electron mobility (c, d) in AIMD snapshots at a 3.0 and 11.1 MPM sampled every 2 fs using the revPBE0-D3 functional. In the top panels (a, b), blue represents electrolyte states and orange represents metallic states, with the intensity of the colour indicating the DoS near the Fermi level (E_F , marked by the black dashed line). The DoS data are normalised such that the maximum displayed value is 1, with values exceeding 1 set to 1 to enhance contrast, consistently across all panels. The bottom panels (c, d) show the corresponding time evolution of the electron mobility, reflecting fluctuations between metallic and electrolyte states.



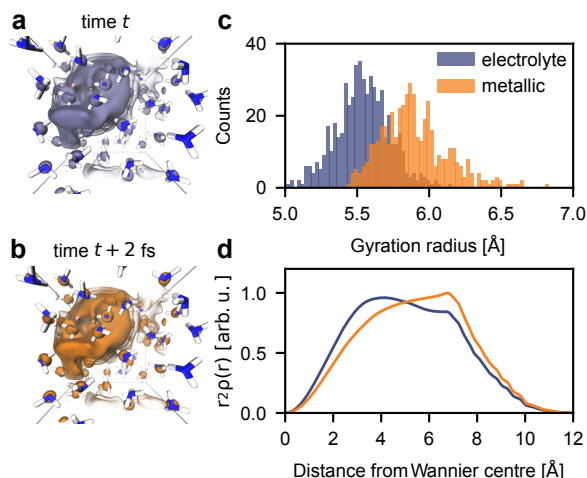
Supplementary Figure 22. Temporal evolution of the DoS (panel a) and electron mobility (panel b) in AIMD snapshots at 6.0 MPM sampled every 2 fs using the revPBE0-D3 functional. In the top panel a, blue represents electrolyte states and orange represents metallic states, with the intensity of the colour indicating the DoS near the Fermi level (E_F , marked by the black dashed line). The DoS data are normalised such that the maximum displayed value is 1, with values exceeding 1 set to 1 to enhance contrast, consistently across all panels. The bottom panel b shows the corresponding time evolution of the electron mobility, reflecting fluctuations between metallic and electrolyte states.

Suppl. Note 5.3 Excess electron density

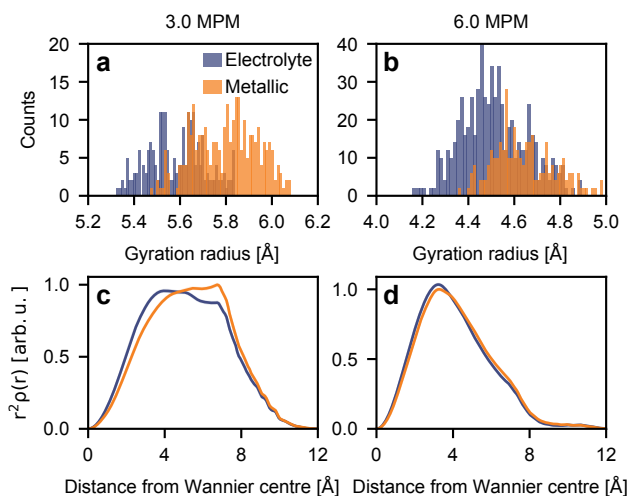
Figure 23 summarises the analysis of the (de)localization behaviour of the solvated dielectron in bulk liquid ammonia, consistent with the results in Figure 3 of the main text, which were calculated with revPBE38-D3. Panels (a) and (b) illustrate electron density for consecutive electrolyte and metallic configurations, showing significant overlap and suggesting that the transition between states involves only subtle shifts in electron localization.

Panels (c) and (d) analyse the spatial extent of the excess electron using 1000 AIMD snapshots at 20-fs intervals, calculated with revPBE0-D3, with data split into metallic and electrolyte states. Panel (c) shows the gyration radius distributions for each state, revealing a bimodal distribution; metallic configurations exhibit larger average gyration radii, indicating a more delocalized electron distribution compared to electrolyte configurations. Panel (d) displays the radial distribution profiles of excess electron density from the Wannier centre, averaged separately for metallic and electrolyte states. The profile for the metallic state is slightly more extended than that for the electrolyte state, highlighting a modest but consistent difference in the spatial extent of the electron between these configurations.

Figure 24 presents an analysis of the (de)localization behaviour of the solvated dielectron, similar to that shown in Figure 23, but based on 500 AIMD snapshots at 2-fs intervals and including data for both 3.0 and 6.0 MPM concentrations, calculated with the same revPBE0-D3 functional. The results are consistent with those in Figure 23, showing bimodal distributions of gyration radii for metallic and electrolyte states, with metallic configurations displaying a larger average gyration radius. At 6.0 MPM, the bimodality is less pronounced. The spherically integrated electron density profiles, derived from Wannier orbital representations, also reveal slightly more extended distributions for metallic states compared to electrolyte states.



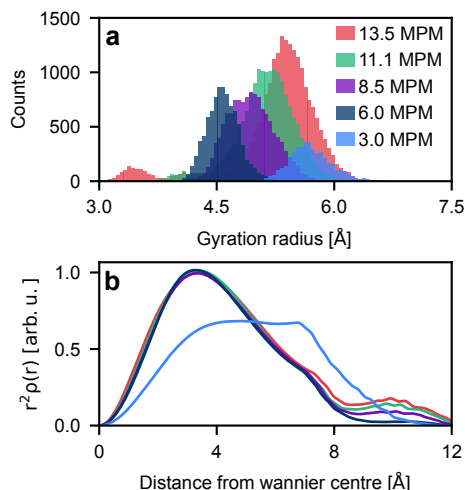
Supplementary Figure 23. Analysis of solvated dielectron density and volumetric properties in 3.0 MPM alkali metal-ammonia solution obtained with revPBE0-D3 functional. Panels (a) and (b) depict the electron density configurations of the dielectron in the electrolyte and metallic states, respectively, with snapshots taken 2 fs apart. Panel (c) displays the radii of gyration, and Panel (d) illustrates the spherically integrated electron density profiles.



Supplementary Figure 24. Analysis of solvated dielectron density and volumetric properties in 3.0 and 6.0 MPM alkali-metal ammonia solution taken from 500 AIMD snapshots at 2-femtosecond intervals obtained with revPBE0-D3 functional. Panels (a,b) displays the radii of gyration, and panels (c,d) illustrates the spherically integrated electron density profiles.

To examine the EMT transition in terms of the structure of the excess electron density, we analysed 4176, 4330, 4159, 4218, and 4176 snapshots sampled at 5-femtosecond intervals from the 3.0, 6.0, 8.5, 11.1, and 13.5 MPM AIMD trajectories (Figure 25). The data reveal significant variations in the gyration radii of single dielectrons. At a concentration of 3.0 MPM, the gyration radius is around 5.7 Å. When the concentration is increased to 6.0 MPM (2 dielectrons), the dielectrons likely experience mutual repulsion or localisation effects due to counter ions, resulting in a reduced gyration radius of 4.6 Å.

As the concentration increases further, the gyration radii steadily rise to 4.9, 5.1, and 5.3 Å at 8.5, 11.1, and 13.5 MPM, respectively, indicating increased delocalisation with higher concentrations. However, small but non-negligible populations with gyration radii around 3.5 Å (for 13.5 MPM) and 4.1 Å (for 11.1 MPM) suggest structural inhomogeneities in the system at higher concentrations.



Supplementary Figure 25. The analysis of structural properties of an alkali-metal ammonia solution across concentrations ranging from 3.0 – 13.5 MPM obtained with revPBE0-D3 functional. The top panel (a) illustrates the radii of gyration, while the bottom panel (b) provides the spherically integrated electron density profiles.

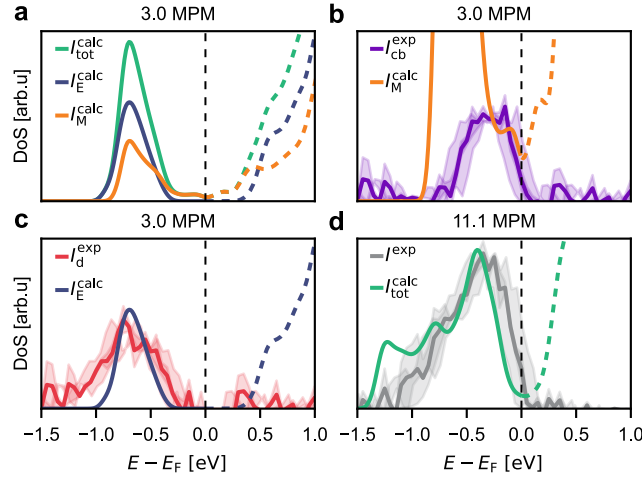
Suppl. Note 5.4 Experimental validation

Here, we examine the density of states (DoS) obtained from G_0W_0 calculations starting from revPBE0-D3 wave functions, in contrast to the revPBE38-D3 based DoS shown in the main text (Figure 5).

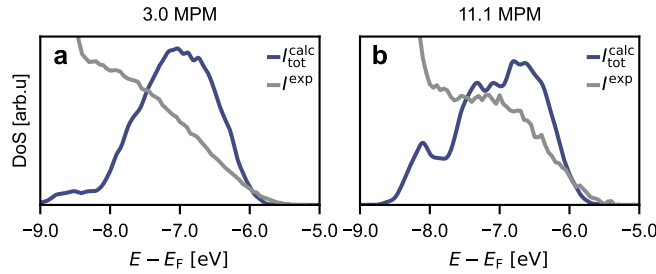
Figure 26 shows the DoS calculated from G_0W_0 starting from revPBE0-D3 wave functions, using 100 AIMD snapshots sampled every 200 fs from four trajectories at 3.0 and 11.1 MPM, alongside experimental data [28] for direct comparison.

The calculated DoS matches well with experimental spectra at similar concentrations of 3.4 and 9.7 MPM. At the higher concentration, where the system is fully metallic, both experiment and simulation display an asymmetric conduction band peak (Figure 26d), ending sharply at the Fermi level (with a slight offset of 0.2 eV due to experimental calibration limits). At the lower concentration, the simulated DoS can be decomposed into electrolyte and metallic contributions (Figure 26a), though experimental spectra represent a time-averaged signal. After accounting for plasmonic features, the experimental signal can similarly be split into localized dielectrons (Figure 26c) and delocalized metallic electrons (Figure 26b). The electrolyte component from simulations aligns well with the experimental dielectron peak, while the metallic component, despite comprising a mix of localised and delocalised states, correlates closely with the metallic part of the experimental spectrum.

In Figure 27, the calculated DoS from G_0W_0 calculations is compared with experimental photoelectron spectroscopy data for alkali-metal ammonia solutions at 3.0 and 11.1 MPM. The figure illustrates that the calculated DoS not only matches well with the experimental data at high concentrations (11.1 MPM vs. 9.7 MPM) but also captures the distinct features of the $3a_1$ valence peak of liquid ammonia.



Supplementary Figure 26. Comparative analysis of the calculated DoS by G_0W_0 method starting from revPBE0-D3 wave functions with experimental PE spectroscopy data for an alkali metal-ammonia solution at two concentrations. (a) calculated DoS at 3.0 MPM, split into metallic (orange) and electrolyte (blue) contributions, alongside the total DoS (green). (b) comparison of the calculated metallic contribution (orange) with the experimental PE spectra of the isolated conduction band (purple). (c) calculated electrolyte contribution (blue) versus the experimental PE spectra of the dielectron only (red). Panel (d) compares the total DoS at an elevated concentration of 11.1 MPM (green) with experimental results at 9.7 MPM (grey). The shaded grey regions in all panels represent confidence intervals, estimated from the relative root mean square deviation (RMSD) between the fits and the scattered experimental data. The experimental data, obtained from reference [28], were fitted using a free-electron gas model combined with a Gaussian function to account for solvated di-electron peaks.

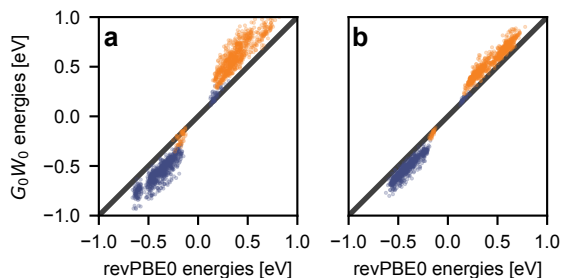


Supplementary Figure 27. Comparative analysis of the calculated DoS by G_0W_0 method starting from revPBE0-D3 wave functions with experimental photoelectron spectroscopy data for an alkali-metal ammonia solution at two concentrations. Panel (a) shows the total calculated DoS at 3.0 MPM, compared with the experimental photoelectron spectrum measured at 3.4 MPM. Panel (b) shows the calculated spectrum at 11.1 MPM and the corresponding experimental spectrum at 9.7 MPM. The experimental data were obtained from Ref. [28].

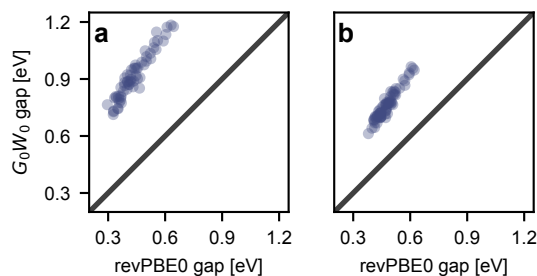
Suppl. Note 5.5 Correlations

In the following, we compare the calculated data employing the revPBE0-D3 hybrid functional with the G_0W_0 method starting from the revPBE0-D3 wave function. Figures 28, 29, and 30 depict the correlations of the orbital energies (on a $2 \times 2 \times 2$ k-point mesh), the band gap energies (on a $2 \times 2 \times 2$ k-point mesh), and the charge carrier mobilities, respectively, for the 3.0 and 6.0 MPM systems.

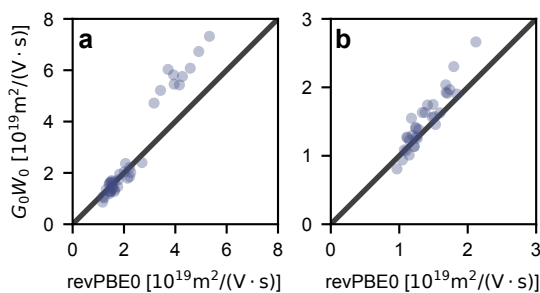
A strong correlation between the two methods is evident across all selected snapshots. This is clearly demonstrated by the comparison of the simulation data in Figures 28, 29, 30 with the black line, which represents $y=x$.



Supplementary Figure 28. Correlation of G_0W_0 versus revPBE0-D3 orbital energies on a $2 \times 2 \times 2$ k-point mesh for both 3.0 (a) and 6.0 MPM (b) systems, considering only the valence band and conduction band. The black line represents $y=x$, highlighting the strong correlation between the data sets.



Supplementary Figure 29. Correlation of G_0W_0 versus revPBE0-D3 band gap energies on a $2 \times 2 \times 2$ k-point mesh for both 3.0 (a) and 6.0 MPM (b) systems. AIMD snapshots with no band gap were excluded from the analysis. The black line represents $y=x$, highlighting the strong correlation between the data sets.



Supplementary Figure 30. Correlation of G_0W_0 versus revPBE0-D3 charge carrier mobilities for both 3.0 (a) and 6.0 MPM (b) systems. The black line represents $y=x$, highlighting the strong correlation between the data sets.

Supplementary References

- (1) Johnson, W. C.; Meyer, A. W.; Martens, R. D. *The Density of Solutions of Alkali Metals in Liquid Ammonia*. *Journal of the American Chemical Society* **1950**, 72, 1842–1843,
- (2) Chakraborty, D.; Chandra, A. *Voids and necks in liquid ammonia and their roles in diffusion of ions of varying size*. *Journal of Computational Chemistry* **2012**, 33, 843–852,
- (3) Berendsen, H.; van der Spoel, D.; van Drunen, R. *GROMACS: A message-passing parallel molecular dynamics implementation*. *Computer Physics Communications* **1995**, 91, 43–56,
- (4) Kresse, G.; Hafner, J. *Ab initio molecular dynamics for liquid metals*. *Phys. Rev. B* **1993**, 47, 558–561,
- (5) Kresse, G.; Hafner, J. *Ab initio molecular-dynamics simulation of the liquid-metal–amorphous-semiconductor transition in germanium*. *Phys. Rev. B* **1994**, 49, 14251–14269,
- (6) Kresse, G.; Furthmüller, J. *Efficiency of ab-initio total energy calculations for metals and semiconductors using a plane-wave basis set*. *Computational Materials Science* **1996**, 6, 15–50,
- (7) Kresse, G.; Furthmüller, J. *Efficient iterative schemes for ab initio total-energy calculations using a plane-wave basis set*. *Phys. Rev. B* **1996**, 54, 11169–11186,
- (8) Perdew, J. P.; Burke, K.; Ernzerhof, M. *Generalized Gradient Approximation Made Simple*. *Phys. Rev. Lett.* **1996**, 77, 3865–3868,
- (9) Adamo, C.; Barone, V. *Toward reliable density functional methods without adjustable parameters: The PBE0 model*. *The Journal of Chemical Physics* **1999**, 110, 6158–6170,
- (10) Zhang, Y.; Yang, W. *Comment on “Generalized Gradient Approximation Made Simple”*. *Phys. Rev. Lett.* **1998**, 80, 890–890,
- (11) Goerigk, L.; Grimme, S. *A thorough benchmark of density functional methods for general main group thermochemistry, kinetics, and noncovalent interactions*. *Phys. Chem. Chem. Phys.* **2011**, 13, 6670–6688,
- (12) Grimme, S.; Antony, J.; Ehrlich, S.; Krieg, H. *A consistent and accurate ab initio parametrization of density functional dispersion correction (DFT-D) for the 94 elements H–Pu*. *The Journal of Chemical Physics* **2010**, 132, 154104,
- (13) Kostal, V.; Mason, P. E.; Martinez-Seara, H.; Jungwirth, P. *Common Cations Are Not Polarizable: Effects of Dispersion Correction on Hydration Structures from Ab Initio Molecular Dynamics*. *The Journal of Physical Chemistry Letters* **2023**, 14, PMID: 37140439, 4403–4408,
- (14) Blöchl, P. E. *Projector augmented-wave method*. *Phys. Rev. B* **1994**, 50, 17953–17979,
- (15) Kresse, G.; Joubert, D. *From ultrasoft pseudopotentials to the projector augmented-wave method*. *Phys. Rev. B* **1999**, 59, 1758–1775,
- (16) Ricci, A.; Ciccotti, G. *Algorithms for Brownian dynamics*. *Molecular Physics* **2003**, 101, 1927–1931,
- (17) Hedin, L. *New Method for Calculating the One-Particle Green’s Function with Application to the Electron-Gas Problem*. *Phys. Rev.* **1965**, 139, A796–A823,
- (18) Hybertsen, M. S.; Louie, S. G. *Electron correlation in semiconductors and insulators: Band gaps and quasiparticle energies*. *Phys. Rev. B* **1986**, 34, 5390–5413,
- (19) Liu, P.; Franchini, C.; Marsman, M.; Kresse, G. *Assessing model-dielectric-dependent hybrid functionals on the antiferromagnetic transition-metal monoxides MnO, FeO, CoO, and NiO*. *Journal of Physics: Condensed Matter* **2019**, 32, 015502,
- (20) Golze, D.; Dvorak, M.; Rinke, P. *The GW Compendium: A Practical Guide to Theoretical Photoemission Spectroscopy*. *Frontiers in Chemistry* **2019**, 7,
- (21) Marom, N. *Accurate description of the electronic structure of organic semiconductors by GW methods*. *Journal of Physics: Condensed Matter* **2017**, 29, 103003,
- (22) Maggio, E.; Liu, P.; van Setten, M. J.; Kresse, G. *GW100: A Plane Wave Perspective for Small Molecules*. *Journal of Chemical Theory and Computation* **2017**, 13, PMID: 28094981, 635–648,
- (23) Van Setten, M. J.; Caruso, F.; Sharifzadeh, S.; Ren, X.; Scheffler, M.; Liu, F.; Lischner, J.; Lin, L.; Deslippe, J. R.; Louie, S. G.; Yang, C.; Weigend, F.; Neaton, J. B.; Evers, F.; Rinke, P. *GW100: Benchmarking G0W0 for Molecular Systems*. *Journal of Chemical Theory and Computation* **2015**, 11, PMID: 26642984, 5665–5687,
- (24) Gerosa, M.; Bottani, C. E.; Valentin, C. D.; Onida, G.; Pacchioni, G. *Accuracy of dielectric-dependent hybrid functionals in the prediction of optoelectronic properties of metal oxide semiconductors: a comprehensive comparison with many-body GW and experiments*. *Journal of Physics: Condensed Matter* **2017**, 30, 044003,
- (25) Monkhorst, H. J.; Pack, J. D. *Special points for Brillouin-zone integrations*. *Phys. Rev. B* **1976**, 13, 5188–5192,
- (26) Madsen, G. K.; Carrete, J.; Verstraete, M. J. *BoltzTraP2, a program for interpolating band structures and calculating semi-classical transport coefficients*. *Computer Physics Communications* **2018**, 231, 140–145,

- (27) Ricci, F.; Chen, W.; Aydemir, U.; Snyder, G. J.; Rignanese, G.-M.; Jain, A.; Hautier, G. *An ab initio electronic transport database for inorganic materials*. *Scientific data* **2017**, *4*, 1–13,
- (28) Buttersack, T. et al. *Photoelectron spectra of alkali metal-ammonia microjets: From blue electrolyte to bronze metal*. *Science* **2020**, *368*, 1086–1091,
- (29) Zurek, E.; Edwards, P. P.; Hoffmann, R. *A Molecular Perspective on Lithium–Ammonia Solutions*. *Angewandte Chemie International Edition* **2009**, *48*, 8198–8232,
- (30) Pizzi, G. et al. *Wannier90 as a community code: new features and applications*. *Journal of Physics: Condensed Matter* **2020**, *32*, 165902,
- (31) Stratt, R. M.; Xu, B.-C. *Band structure in a liquid*. *Phys. Rev. Lett.* **1989**, *62*, 1675–1678,
- (32) Wang, L.-W.; Bellaiche, L.; Wei, S.-H.; Zunger, A. “Majority Representation” of Alloy Electronic States. *Phys. Rev. Lett.* **1998**, *80*, 4725–4728,
- (33) Zheng, C.; Yu, S.; Rubel, O. *Structural dynamics in hybrid halide perovskites: Bulk Rashba splitting, spin texture, and carrier localization*. *Phys. Rev. Mater.* **2018**, *2*, 114604,
- (34) Rubel, O.; Bokhanchuk, A.; Ahmed, S. J.; Assmann, E. *Unfolding the band structure of disordered solids: From bound states to high-mobility Kane fermions*. *Phys. Rev. B* **2014**, *90*, 115202,
- (35) Nosé, S. *A unified formulation of the constant temperature molecular dynamics methods*. *The Journal of Chemical Physics* **1984**, *81*, 511–519,
- (36) Hoover, W. G. *Canonical dynamics: Equilibrium phase-space distributions*. *Phys. Rev. A* **1985**, *31*, 1695–1697,
- (37) Schewe, H. C.; Brezina, K.; Kostal, V.; Mason, P. E.; Buttersack, T.; Sterner, D. M.; Seidel, R.; Quevedo, W.; Trinter, F.; Winter, B., et al. *Photoelectron Spectroscopy of Benzene in the Liquid Phase and Dissolved in Liquid Ammonia*. *The Journal of Physical Chemistry B* **2021**, *126*, 229–238.
- (38) Thürmer, S.; Malerz, S.; Trinter, F.; Hergenbahn, U.; Lee, C.; Neumark, D. M.; Meijer, G.; Winter, B.; Wilkinson, I. *Accurate vertical ionization energy and work function determinations of liquid water and aqueous solutions*. *Chem. Sci.* **2021**, *12*, 10558–10582,
- (39) Winter, B.; Thürmer, S.; Wilkinson, I. *Absolute Electronic Energetics and Quantitative Work Functions of Liquids from Photoelectron Spectroscopy*. *Accounts of Chemical Research* **2023**, *56*, 77–85,
- (40) Pugini, M.; Credidio, B.; Walter, I.; Malerz, S.; Trinter, F.; Sterner, D.; Hergenbahn, U.; Meijer, G.; Wilkinson, I.; Winter, B.; Thürmer, S. *How to measure work functions from aqueous solutions*. *Chem. Sci.* **2023**, *14*, 9574–9588,